Optimisation of additively manufactured coiled flow inverters for continuous viral inactivation processes

Maria Cecilia Barrera [a], Damien Leech [b], Aleksandar Josifovic [a], Anita Tolouei [c], Gareth Alford [d], Martin J. Wallace [e], Nicholas Bennett [f], Ricky Wildman [b,g], Derek J. Irvine [b,g], Anna Croft [h], Ender Özcan [i], Alastair J. Florence [a], Blair Johnston [a], John Robertson [a], Cameron J. Brown [a,*]

[a] Strathclyde Institute of Pharmacy & Biomedical Science, University of Strathclyde, Glasgow G1 1RD, UK
[b] Centre for Additive Manufacturing, Faculty of Engineering, University of Nottingham, Nottingham NG7 2RD, UK
[c] Vaccines Technical Research and Development, GSK, Rockville, MD, USA
[d] Technology Translation, GSK, Stevenage SG1 2NY, UK
[e] Innovation and Manufacturing Technology, GSK, Dublin D24 K11, Ireland
[f] School of Chemistry, University of Nottingham, Nottingham NG7 2RD, UK
[g] Department of Chemical and Environmental Engineering, Faculty of Engineering, University of Nottingham, Nottingham NG7 2RD, UK
[h] Department of Chemical Engineering, Loughborough University, Loughborough LE11 3TU, UK
[i] School of Computer Science, University of Nottingham, Nottingham NG8 1BB, UK

ABSTRACT

This article reports the development and utilisation of an adaptive design workflow methodology for use as a platform technology for the printing, testing, and optimisation of biopharmaceutical processing reactors. This design strategy was developed by application to the complex structure of the coiled flow inverter (CFI). In this way, the many possible physical parameters of the reactor were optimised, via a combination of experimental results, computational fluid dynamics and machine learning approaches, to find the CFI setups that provide the optimal flow properties for a particular application. Additively manufactured reactors are seeing increasing interest in the field of biopharmaceutical production. This is because the desired output volumes are typically small and there is an increasing move towards adopting continuous production, to replace traditional batch production. This approach allows for the tailoring of reactors for a specific reaction, i.e. attempting to maximise the desired aspects of the reaction through refinement of the physical parameters of the reactor, so creating a large possible parameter space to explore. Consequently, the holistic optimisation of CFI reactors and 3D printing is established as providing better plug flow mixing relative to traditional tube coiled reactors. In addition, a trained metamodel in combination with multilayer equations is demonstrated to predict reactor performance quickly and accurately.

1. Introduction

Application of CFI reactors in chemical industry is proven to increase the process performance in terms of synthesis (Tomar et al., 2023) and reaction times (Sharma et al., 2016). Traditional coiled flow inverter (CFI) reactors are constructed by coiling tubing around a 'backbone' structure made of PVC piping, which constrains values of the coil diameter and inner diameter to the sizes of piping commonly available (1/16" (1.6 mm), 1/8" (3.2 mm), ¼" (6.4 mm) etc.). Having discrete tubing sizes greatly limits the design space and may even limit our ability to create the most suitable design for a process application. Coiled structure is commonly used in reaction chemistry but in most cases it's limited to single coil (Pal et al., 2019) or 4-coil (Schael et al., 2024) constructs. In addition to this, the construction of this traditional backbone structure for a multi-layer structure can be time-consuming, labour intensive and cannot be easily modified once constructed. Alternatively, 3D printing of individual, modular reactors alleviates many of these issues, as a reactor can be manufactured and tested as a standalone device or connected in series using simple plastic tubing connectors to produce a larger multi-layer setup. Individual layers can be swapped out for freshly printed reactors if they get damaged, and the

Nomenclature

List of abbreviations and acronyms

d_c	coil's diameter
d_i	internal diameter of the coil's tubing
h_c	height of the coil ($n_t \times p$)
n_b	number of 90-degree bends per reactor element
n_t	number of turns per coil
R_w	relative width parameter
T^*	modified torsion parameter
$t_{5\%}$	time at which $F(t) = 0.05$
$t_{95\%}$	time at which $F(t) = 0.95$
t_m	mean residence time
σ^2	variance
ΔP	pressure drop

$C(t)$	conductivity as a function of time
D	diffusion constant
Dn	Dean number
$E(t)$	residence time distribution function
f	friction factor
$F(t)$	cumulative distribution function
L	path's length
p	pitch of the coil
Re	Reynolds number
u	mean velocity
μ	dynamic viscosity
ν	kinematic viscosity
ρ	density
τ	space time

reactor size can easily be increased by adding extra layers. On the other hand, there can be restrictions with the build volume of the additive manufacturing platform limiting the size of the reactors and the post-processing time required for each reactor. This problem of CFIs lends itself well to the process of additively manufactured reactors, in which meso- or milli-fluidic reactors can be rapidly fabricated, over the course of hours, and tested the same day. This high throughput fabrication works particularly well for the design of CFIs for viral inactivation, as this allows the building of long residence time devices in a matter of days, with less of the repetitive fabrication of traditional CFIs, that can lead to unintentional variations and inconsistencies in the design.

The optimal reactor for a specific process depends not only on the desired outcome but also on the input conditions and physical constraints of the problem, such as the flow rate, residence time, maximal pressure, and available working volume. Consequently, many design options may need to be evaluated, through simulation and/or experiment, to better understand how all these factors influence the reactor's performance. With this understanding, an adaptive design approach is proposed – a workflow focused on a cycle of design, testing and optimisation of a reactor to enhance a particular process. Systematically exploring an initial design space is a very time-consuming task, and thus, a lot of time and effort can be saved using a mathematical model that correlates a reactor's performance with its geometrical and flow properties.

In this work, we present a meta-model (MM) for R_w trained using experimental and Computational Fluid Dynamics (CFD) simulations, and then we use this MM to calculate an optimal reactor for a specific case study.

The overall objective of this work is to demonstrate how the biopharmaceutical industry can move to bespoke single-use 3D printed reactors by presenting:

1. 3D printing technology that will explore wider design space (see Sections 1.1.1 and 1.1.3 for design space parameters and performance indicators, respectively).
2. Systematic design space analysis to explore full-factorial range of design parameters.
3. Validated design solutions via numerical CFD simulation.
4. Validated design solutions using bespoke experimental measurements.
5. An equation based meta-model that will accurately estimate design performance of any given CFI reactor.

1.1. Coiled flow inverters

1.1.1. Design of the coiled flow inverters

The coiled flow inverter (CFI) itself is a type of reactor device in which four tubular coils are situated at 90° to one another. The bends produced by this layout disturb unmixed regions and the helical regions cause radial mixing through the formation of Dean vortices. The CFI design has been used in a variety of processes, including heat transfer (Kumar et al., 2007a, b), nanoparticle production (Wu and Torrente-Murciano, 2018; Pophali et al., 2022) and liquid-liquid extraction (Gürsel et al., 2016). Another process they are heavily used in is low pH viral inactivation (Orozco et al., 2017; Parker et al., 2018; David et al., 2019, 2020), in which biopharmaceutical pre-cursors and products are made safer through slow mixing with a low pH component, over the course of a long time period. This lends itself well to CFI design due to their ability to induce non-turbulent mixing, their often narrow residence time distributions (RTD) and ability to be stacked in series to produce long fluid flow routes (Gaddem et al., 2022; Klutz et al., 2016; Parker et al., 2018; David et al., 2019, 2020; Orozco et al., 2017). Designing and constructing a CFI module is complex due to the multitude of physical parameters, such as flow rates, pressure requirements, and thermal properties, along with the extensive tubing lengths often necessary to achieve optimal functionality. Traditional CFIs, in biopharmaceutical applications, are built from plastic tubing wrapped around a 'backbone' structure that produces the helical coils and are usually made by hand (although other construction materials are available (Kumar et al., 2007a, b). In addition to the labour intensive construction, many of the most important parameters are interlinked and so the choice of an optimal CFI design is situationally dependent on both the exact desired outcome and the material properties of the fluids within the reactor. Previous work has looked into creating relationship between number of bends and total volume to achieve near plug flow (Saxena and Nigam., 1984), however this is not sufficient for more complicated multi-layer constructs.

The physical structure of a generic CFI is defined by key parameters of (Klutz et al., 2015):

- Internal diameter of tubing d_i
- Diameter of coil d_c
- Height of coil h_c
- Pitch of coil p: axial distance between two adjacent turns of the coil, measured from tube centre to tube centre.
- Number of turns n_t per coil.
- Number of 90° bends n_b per reactor element.

where three terms are intrinsically linked via $n_t = h_c/p$. However, with a traditional CFI design of four coils at 90° to one another, reactor

element sets $n_b = 4$ and thus, CFI's can be defined instead by d_i, d_c and any two of h_c, p and n_t. This collection of four coils at 90° to one another is often referred to as a 'layer', alluding to their ability to be easily stacked to produce a longer flow route.

Overall, we sought to design an additively manufactured coiled flow inverter reactor, suitable for use in low pH viral inactivation processes. To maximise the efficiency of viral inactivation, the desired output parameters of such a device are a narrow residence time distribution (RTD), to ensure slow but thorough mixing, and low pressure drop, due to the long residence times required for this process (Kateja et al., 2021).

1.1.2. Flow properties of a CFI reactor

The RTD of such a CFI is driven primarily by the formation of Dean vortices and the 90° bends (Schmalenberg et al., 2019). Centrifugal forces along the helices push the flow forces outward and the 90° bends ensure no regions of the cross-sectional profile are unaffected by this shift and left un-mixed. Due to these centrifugal forces, the Dean vortices formed are shifted and break their standard symmetry (Saxena and Nigam, 1983; Vashisth and Nigam, 2008), with the amount of asymmetry dependent on the fluid and flow properties. These flow properties can be described primarily by two dimensionless parameters: the Dean number Dn and the modified torsion parameter T^*, (Mandal et al., 2011).

$$Dn = \mathrm{Re}\sqrt{\frac{d_i}{d_c}}, \tag{1}$$

$$T^* = \mathrm{Re}\frac{\pi d_c}{p} \tag{2}$$

respectively (Schmalenberg et al., 2019), where Re is the Reynolds number, related to the mean velocity u, the inner diameter d_i and the kinematic viscosity υ by:

$$\mathrm{Re} = \frac{ud_i}{\upsilon} \tag{3}$$

1.1.3. Measurement of CFI reactor performance

To define a measurement of the efficacy of a particular combination of CFI parameters, the relative width parameter (R_w) (Klutz et al., 2015) is used. This relies on standard residence time distribution experiments, in which a tracer is either pulse or step flowed through a reactor and the concentration tracked as it passes through a specific point, designated as the outlet. The overall distribution is characteristic of the mixing that takes place within the reactor. A step injection approach was used to study RTD curves, and since the conductivity of the tracer is directly proportional to its molar concentration, the experimental cumulative distribution $F(t)$ was calculated using Eq. (4), where $C(t)$ and C_0 are the conductivity at time t and the inlet conductivity, respectively.

$$F(t) = \frac{C(t)}{C_0} \tag{4}$$

An example of an $F(t)$ curve can be found in Fig. S1. This function is also related to the residence time distribution function $E(t)$ through Eq. (5):

$$E(t) = \frac{dF(t)}{dt} \tag{5}$$

From the cumulative function, we can obtain relative width, R_w, which defines the 'compactness' of the RTD:

$$R_w = \frac{t_{5\%}}{t_{95\%}} \tag{6}$$

where $t_{5\%}$ and $t_{95\%}$ are the times at which $F(t) = 0.05$ and $F(t) = 0.95$, respectively. Higher R_w values represent better mixing inside the reactor, and thus an ideal plug flow reactor has an R_w value of 1.

The frictional pressure drop can be obtained using Eq. (7):

$$\Delta P = f\frac{\rho L}{2 \; d_i} \; u^2 \tag{7}$$

where ρ is the fluid's density, L is the path length and f is the friction factor. The path length is the linear length of the coil (i.e. the length of the coil after it has been pulled into a straight line) and it is calculated as $n_t\sqrt{(\pi d_c)^2 + p^2}$. Different empirical equations can be used to calculate the friction factor in a coiled flowed reactor, like for example Eqs. (8) and (9) (Schmalenberg et al., 2018).

$$f = \frac{64}{\mathrm{Re}} \; [1 + 0.0456 \; Dn^{0.603}] \tag{8}$$

$$f = \frac{64}{\mathrm{Re}}[1 + 0.033(\log_{10}(Dn))^4] \tag{9}$$

The relative width value, alongside the pressure drop, is the primary comparison point when comparing differing CFIs with varied physical parameters.

2. Materials and methods

2.1. CFD simulation

CFD simulations have been extensively used to characterize CFI reactors' flow properties in other work (Gaddem et al., 2021; Kumar and Nigam, 2005; Soni et al., 2019; Jha et al., 2020; David et al., 2020). The primary input conditions to the CFI reactor process design are the flow rate and desired residence time. This defines the total volume of the reactor and it is up to the process designer to size and shape the tubing accordingly to get the best RTD, whilst maintaining an acceptable pressure drop.

2.1.1. Single-layer reactors

CFD modelling was used as an immediate method of predicting the flow properties of a particular set of physical parameters in a CFI reactor and a method of amassing data to be put towards a larger predictive meta-model. Using COMSOL Multiphysics 6.0, a generic CFI design was built with parametric dependencies that allow the variation of the inner diameter, coil diameter, pitch, number of turns, flowrate and tracer's diffusivity. From this model, the residence time distribution response of specific designs was measured by solving the steady state flow properties and then tracking a step-injection's response at the outlet of the reactor. The tracer used had a concentration of 0.25 mol/m^3 and a diffusion constant of 9.3 10^{-9} m^2/s which corresponds to that of H$^+$ ions (David et al., 2020). Simulated data (outlet concentration vs time) was fitted to a cubic spline using Python3 with the SciPy module to obtain $F(t)$, and then R_w was calculated as the ratio between $t_{5\%}$ and $t_{95\%}$.

2.1.2. Design of experiments – parameters' space

In this work, a full factorial design was carried out using d_i, d_c and n_t as the controllable factors. The levels for n_t were arbitrarily chosen as 5, 6, 8, 10 and 12, and the levels for d_i (4.8 mm, 6.4 mm, 8 mm and 9.6 mm) and d_c (41 mm, 60 mm, 83 mm,107.2 mm and 159.5 mm) were chosen based on pipe sizes commonly used in industry. These 100 combinations were run at three different flow rates (22 ml/min, 66 ml/min and 110 ml/min), resulting in a total of 300 combinations. In all cases, the pitch was set to 1.5 times the internal diameter.

To decrease computational time and obtain designs suitable for 3D printing (Anycubic, Photon Mono X), the 300 reactors in the DoE were scaled down, keeping Re, Dn and T^* constant by multiplying Q, d_i, d_c and p by the same scaling factor (scaling factor was chosen to ensure the scaled reactor had a volume of 10 ml). The scaling-down method is a valid approach since simulated R_w values obtained using full-size reactors are the same as those simulated using their corresponding scaled-down counterparts, as shown in Fig. S2. For other properties, like

volume and pressure drop, values simulated using scaled-down reactors are not equal to those obtained when simulating the full-size designs, however, these values can easily be correlated as shown in Table S1.

2.1.3. Multi-Layer reactors

The multi-layer design within CFD has an additional caveat compared to experiment, which is how to exactly connect the reactor flow routes. In the experimental setup, these regions would consist of connecting tubing and they host many of the probes that are used to harvest data. It is inevitable that this will have some effect on the flow properties of the material moving through the system and therefore the desired outputs.

The set-up shown in Fig. 1a was used to simulate 2-layered reactors,
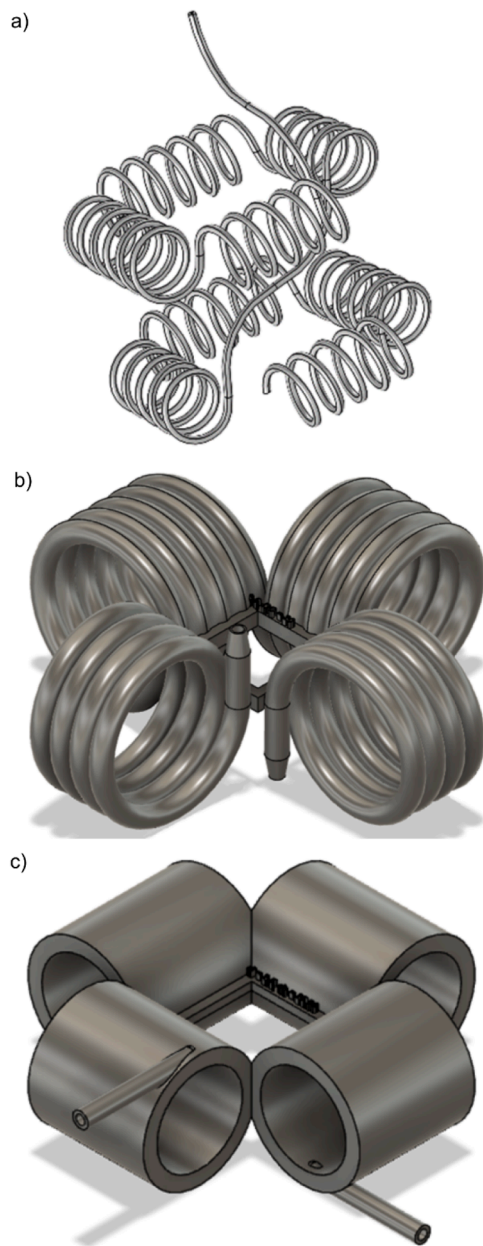
Fig. 1. a) Multi-layer stacking used in the CFD simulations (d_c = 24 mm, d_i = 2.8 mm and p = 10 mm), b) CAD model of a generic four-component coiled flow inverter, displaying all the core parameters and mimicking the traditional ˈcoil wrapped around a coreˈ design. c) Variation of the CFI design, that referred to as the encased CFI, that allows for finer inner and outer diameters and more structural stability when interfacing with flow equipment.

however, this arrangement led to convergence problems when trying to simulate reactors with more layers. For these reactors, each layer was simulated separately, and the output of the previous layer was used as input. This approach significantly reduces computational time, however, it also assumes that the fluid entering the reactor is perfectly mixed in the radial direction, which is a simplification. To validate this methodology, the *RTD* of a 2-layered reactor was compared to that obtained using the entire 2-layered reactor, and results are shown in Fig. S3. The R_w values obtained using both methods differ by less than 1 %.

2.2. Additively manufactured coiled flow inverters

2.2.1. Process – stereolithography (SLA)

Additively manufacturing reactors has long been an area of interest within many regions of chemistry, due to the sheer freedom of design and access to previously inaccessible parameters of variation (Maier et al., 2020; Heidt et al., 2020; Dragone et al., 2013; Grande, 2021). This allows the generation of designs that optimise reactions, based on knowledge of the desired outputs and the material and physical inputs, and can interface with most, if not all, of traditional flow chemistry equipment including syringe pumps, probes and couplings.

Stereolithography (SLA) typically uses a laser to raster and draw an image in the XY plane onto a vat of photocurable resin, before a stage adjusts the object in the Z plane and begins a new layer. These photocurable resins use photoinitiators that are active in the UV to visible range, with 405 nm being the most common active wavelength. Recent years have shown alternative methods of directing the light into the vat of resin that are faster, whilst still maintaining the elevated level of quality that SLA is known for. LCD printers (or Digital Light Processing, DLP), in which an LCD (liquid crystal display) acts as a photomask between a static UV source and the resin vat, are known to be reliable, cheap and fast, due in part to their ability to cure an entire layer all at once and their low unit cost. Much work has been undertaken in printing reactors, across multiple scales and even with designs similar to coiled flow inverters (in both the coiled and backbone structures) (McDonough et al., 2019a, 2019b; Bobers et al., 2020; Kováts et al., 2020; Wu and Torrente-Murciano, 2018). DLP 3D printing was used to fabricate a variety of reactors, including a facsimile of the coiled flow inverter. For completeness, it should also be noted that a range of other manufacturing techniques are available for printing reactors, including sintering of metals (Norman et al., 2023; Grande and Didriksen, 2021) and two-photon polymerisation of silica glass (Bauer et al., 2023).

2.2.2. Design process – CAD and parametric design

Based on the workflow defined previously, adaptable designs are paramount to the process. As such, parametric design, in which 3D models are shaped via algorithmic processes, in contrast to direct definitions allow the introduction of quality-of-life changes and quickly vary the designs within parameter space, using desired values of internal diameter, coil diameter and coil length etc. This was achieved primarily within AutoCAD and AutoDesk Fusion 360.

Two core designs were used – the ʻtraditionalʼ and the ʻencasedʼ design, as seen in Fig. 1b and c. The traditional design seeks to replicate the standard design of CFIʼs, involving coiled tubing wrapped around a structure, and maintains a constant inner and outer diameter tube throughout the whole of the flow route. This is fabricated primarily to show how the SLA process can be used to print intricately designed reactors with a high level of accuracy. The encased design improves on the original design, as it removes the necessity of a strictly defined wall diameter and instead simply cuts the coiled flow route from a solid block of material. This means coils can be more tightly pitched than the traditional designs, as thin wall thicknesses, whilst still printable, make for a brittle reactor.

2.2.3. Limitations – resolution, negative feature resolution and build volume

As with any manufacture process, there are inherent limitations. As

already discussed, prints are limited by the build volume available on the printers, however as material is placed further from the central motors that drive the Z-movement of the printer, the success rate is reduced, effectively limiting the build volume to around 80 % of the total volume. Further to that, there is a lower limit imposed by the resolution of the printer in the X-Y plane. This limit is driven by the pixel size provided by the LCD screen within the printer, which is 50×50 microns. However, in practice, achieving a single pixel resolution requires a lengthy tuning process and often a chemical modification to the resin. The resolution can further vary depending on whether the aim is to achieve a positive or negative feature, both of which are required in the production of printed reactors. This, in combination with the post-processing steps described later, ensure that the negative resolution limit is more commonly between 500 and 1000 microns, providing the smallest width flow route we can reliably print long channels of metres in length (Heidt et al., 2020).

2.2.4. Post-processing

One aspect of printing reactors that is somewhat overlooked within the literature is the post-processing of reactors printed using SLA, DLP and LCD processes. The radical polymerisation process that is core to the printing is only partially completed when the print is freed from the build plate. Typical prints would then be exposed to a compressed air/nitrogen purge and/or placed into a isopropanol solvent bath for 3–5 min to remove any additional uncured resin, prior to being moved to a UV curing station that finishes the polymerisation process. The gas purge was primarily used when internal channels were present. This was because the process of clearing the channels becomes more complex due to the possibility of clogging the flow route with uncured resin. Immediately after printing, air/nitrogen was pushed through the reactor to remove and recover as much uncured resin as is possible. Solvent was then pushed through the internal channels, again to remove further uncured resin, and the print was then placed into a solvent bath.

Following that, the internal channels were filled with a residual mixture of air/nitrogen, solvent and uncured resin and therefore still liable to clog if exposed to UV light whilst un-monitored. As such, a cycle of clearing the internal channels with air and water (ensuring the contaminated water was soaked into a solid medium or contained and left to cure in ambient UV), followed by short bursts of UV exposure (60–180 s, depending on the size of the reactor, the longer the flow channels the lower the exposure time), were carried out until the print was dry to the touch.

2.3. Experimental measurements

Even though the theory of mixing inside a CFI reactor has been documented and well-studied over the last few decades, experimental measurement is still regarded as the most accurate way of quantifying residence time distribution. As this work characterises small size 3D printed reactors, many aspects of system design had to be considered to minimise the measurement error and improve reading consistency.

2.3.1. Experimental setup and P&D

The experimental set-up is shown in Fig. 2. This set up consisted of two feed vessels, one contained purified water (water tank) and the other a NaCl solution (tracer tank), connected to a solenoid valve that controlled which fluid entered the reactor (Rossi et al., 2017). Additionally, pressure indicators (PI1 and PI2) were used to detect potential blockage in the system and a Bronkhorst flow metre measured the water tank's flow rate. Finally, the conductivity was measured at the outlet of the reactor using a conductivity probe (Mettler Toledo InPro7100i/12/120/4435) (Mohammadi and Boodhoo, 2012; Toledo, 2017) attached to a bespoke 3D printed flow cell.

Both water and tracer feed pumps were calibrated to dispense identical flow rates. The tracer feed tank was prepared with 1 mol/L of sodium chloride (Roth et al., 1999; Mora Orozco and Jones, 2014),
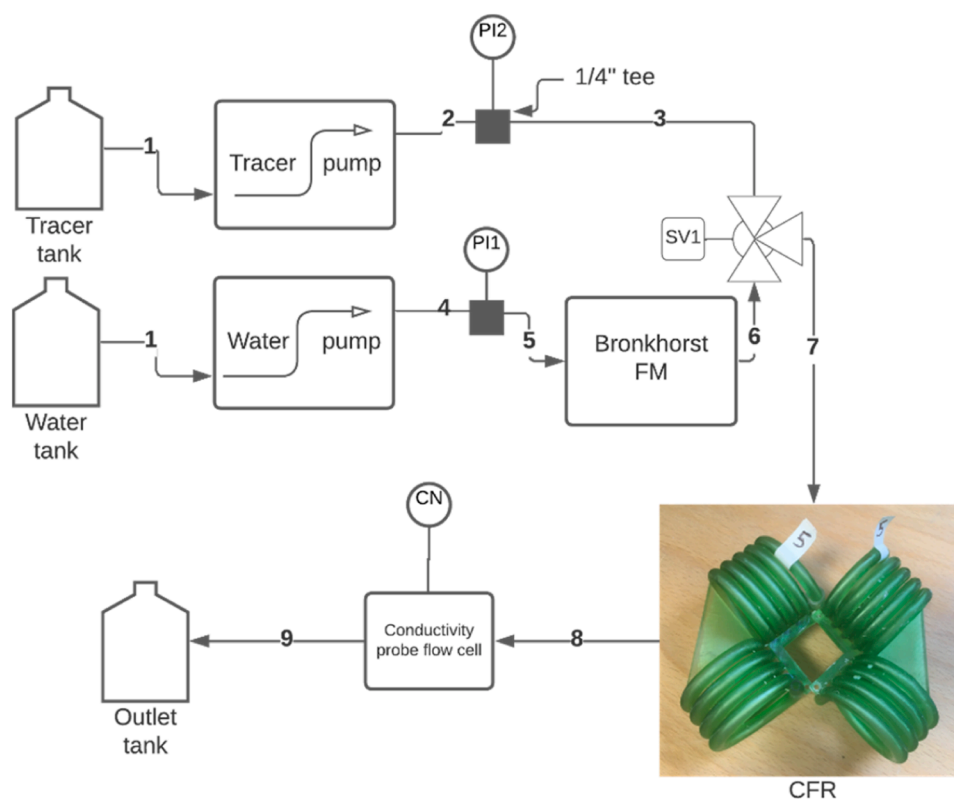
Fig. 2. Schematic of the two-pump setup required to accurately measure the RTD of a CFI reactor. The parameters of the 3D printed reactor shown here are: d_c = 10 mm, d_i = 3.2 mm and p = 7.5 mm.

thoroughly mixed and dissolved in purified water. The cycle started by running purified water through the system to ensure the reactor was primed and no air was trapped in the system. Fig. S7 shows conductivity values vs time and covers the three main steps of the RTD measurement process. This figure also contains a flowrate vs time plot that is used to determine the exact time at which each step starts and ends.

In step 1, purified water is run through the system until the conductivity is below 50 µS/cm. At this point, the solenoid valve switches the fluid entering the reactor from water to tracer until the conductivity reaches a maximum and constant value for at least 120 s (step 2). In step 3, the tracer pump is switched off and the water pump is put back online. The system is then cleaned with purified water until the conductivity is below a set standard (50 µS/cm).

The probes collected data every second via Mettler Toledo M800 and NI Labview USB6212 (Toledo, 2013; NationalInstruments, 2017) - this is the maximum acquisition time advised by the probes' manufacturers for stable and noise-free reading. Mean residence times (τ) are typically of the order of hundreds of seconds, ensuring the error due to acquisition time is usually 1 % or less. The maximum conductivity value can also vary with repeat readings, however, this does not present an issue in the experiments since the conductivity values were normalised.

2.3.2. Calculating R_w of a single layer

For interpolation purposes, the data collected by the conductivity probe was first smoothed out using a Savitzky-Goaly filter (Savitzky and Marcel, 1964) (length of the filter window = 21 and polynomial order = 4) and then fitted to a cubic spline using Python 3 with the SciPy module. An example is shown in Fig. 3, where the red dots represent the experimental readings, and the dashed black line corresponds to the cubic spline. Additionally, the vertical blue lines represent $t_{5\%}$ and $t_{95\%}$, the times when $F(t) = 0.05$ and $F(t) = 0.95$, respectively. Using the 5 % and 95 % times instead of 0.5 % and 99.5 %, as is also used in literature to calculate R_w, reduces the impact undesirable signal fluctuations would have on the final R_w value. To minimise random errors, each run was repeated 4 times. As evidenced in Table S3, the first measurement usually exhibits slightly different results to the rest, likely due to minor pressure differences between water and tracer lines or residual air trapped in the system, and thus, it was not included in the calculation of the averages or standard deviations.

2.3.3. Multi-Layer reactors

Experimental setup for the multi-layer RTD measurement contains 4 printed reactors. Final three layers separated by a conductivity probe, to quantify R_w value changes throughout the flow route inside reactor. ESI
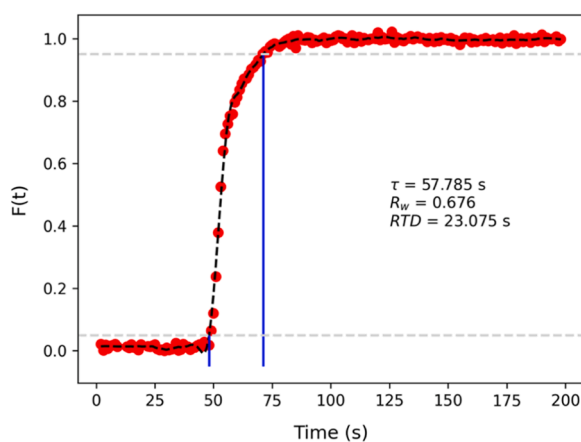
Fig. 3. Experimental $F(t)$ curve. The red dots and the black dashed line represent the measured values and the fitted cubic spline, respectively. The vertical blue lines are $t_{5\%}$ and $t_{95\%}$ and the horizontal grey lines are $F(t) = 0.05$ and $F(t) = 0.95$.

Fig. 7 shows schematic diagram shows location of conductivity probes with respect to individual reactor layers.

2.4. CFI design optimisation

To demonstrate how the meta-models in this work can be incorporated into an optimisation routine, an objective was set to maximise a reactor's R_w. For this demonstration, we selected water as the carrier fluid with a 1 M NaCl tracer and fixed the reactor volume and flowrate to 40.88 L and 2.5 L/min, respectively. Other constraints were also added to assure to printability of the final design.

The optimisation algorithm was constrained to stay inside the meta-models' boundaries and the maximum number of layers was set to 8. Additionally, the coil's internal diameter was constrained to be larger than 0.75 mm, by fixing the maximum Reynolds number accordingly, and the coil's diameter and length were forced to be lower than 20 mm and 30 mm, respectively.

Two of the meta-models' variables are continuous (number of layer and number of turns) and two are discrete (internal diameter and coil diameter). Consequently, a loop approach was used for the discrete variables to obtain all combinations of these variables and then for each of these combinations a steepest descent algorithm was used to find the optimal continuous variables. Starting from the initial guess (X_0), a new point (X_1) was found by searching along the opposite direction of the objective function's gradient $\nabla F(X_0)$:

$$X_1 = X_0 - t \quad \nabla F(X_0) \tag{10}$$

where t is the step length, and it determines the distance the algorithm needs to move along the specified direction. The step length for each iteration was found using 100 equidistant trial steps and selecting the one that returned the lowest function value. This procedure was repeated until either convergence was achieved with a tolerance of 10^{-8} or the maximum number of iterations was reached.

3. Results and discussion

3.1. CFD simulations of single-layer reactors and Meta-models

Out of the 300 simulations in the DoE, 15 failed to converge and thus, the results shown in this section were obtained using 285 different CFI setups. As can be seen in Fig. 4, simulated mean shear rate values are in excellent agreement with Eq. (11), a theoretical equation found in (Berg and van Wunnik, 2017):

$$\overline{\gamma} = \frac{16}{3} \frac{u}{D_i} \tag{11}$$

Furthermore, this Fig. Shows that Eq. (7) with the friction parameter from Eq. (9) can be used to predict simulated pressure drops, and thus, they can be used as a meta-model for this property.

3.1.1. Meta-model for simulated R_w

Simulated R_w values from 228 4-coil reactors obtained using H^+ as the tracer were used to train a multivariate adaptive regression splines (MARS) model (Friedman, 1991; Friedman and Roosen, 1995). The MARS model is a weighted sum of basis functions; where each basis function is a constant, a linear function, a hinge function, or a combination of these elements. Hinge functions have the form $\max(0, x - knot)$ or $\max(0, knot - x)$, where a $knot$ is a constant that divides the parameter's space of the input variable x. The MARS algorithm is able to automatically determine the optimal number of basis functions and their parameters to prevent overfitting and maximise accuracy. Additionally, MARS allows the user to specify the maximum degree of interaction of each term, and in this work, we have chosen a value equal to 2.

A test set of 57 points was used to assess the model's performance, and, as can be seen from Fig. 5, our model performs very well at
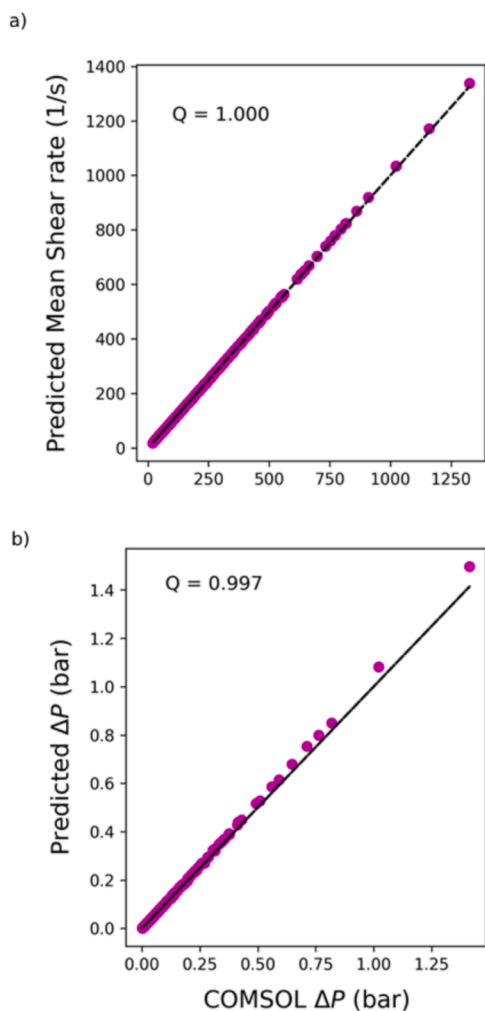
a)

b)

Fig. 4. a) Predicted vs simulated values for the average shear rate of 285 4-coils reactors simulated using a fluid with $\mu = 0.003474$ kg/m/s and $\rho = 966$ kg/m³. Predicted values were obtained using Eq. (11). b) Predicted ΔP, obtained using Eq. (9) to calculate the friction factor, against simulated values.
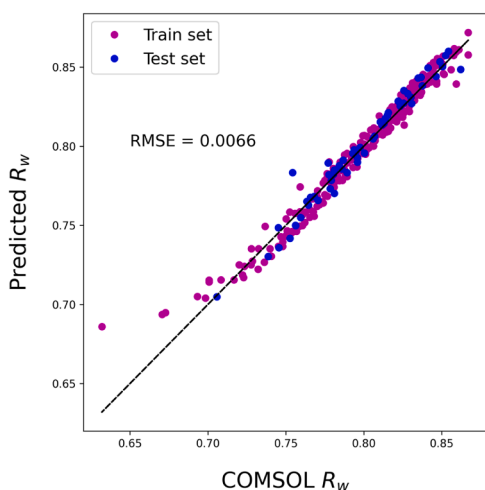

Fig. 5. Predicted vs simulated values for R_w of 285 4-coils reactors simulated using a fluid with a $\mu = 0.003474$ kg/m/s and $\rho = 966$ kg/m³. Parameter ranges were: Re = 13.5–135.2, Dc/Di = 4.38–33.24 and turns = 5–12.

predicting R_w with a RMSE equal to 0.007. However, it is important to emphasise that this meta-model is only valid within the boundaries of the input parameters (Re from 13.5 to 135.22, Dc/Di from 4.4 to 33 and n_t from 5 to 12).

The equation for this model is:

$$
\begin{aligned}
R_{w,MM} = {} & 0.0008834 * X2 * X3 + 6.024 * 10^{-5} * X2 \\
& * \mathrm{MAX}(0, \quad 33.238 - X2) - 5.823 * 10^{-6} \\
& * X1^2 - 3.423 * 10^{-5} * X1 * X3 + 1.471 * 10^{-5} * X1 \\
& * \mathrm{MAX}(0, \quad 33.238 - X2) + 5.230 * X1 \\
& * \mathrm{MAX}(0, X2 - 33.238) + 0.001268 \\
& * X1 - 0.001141 * X3^2 + 0.001035 * X3 \\
& * \mathrm{MAX}(0, \quad 33.238 - X2) - 0.004240 \\
& * \mathrm{MAX}(0, \quad 33.238 - X2) + 0.6410
\end{aligned}
$$

(12)

where, X1 = Re, X2 = Dc/Di and X3 = n_t.

3.1.2. CFD simulations with different fluids

The model can also be expanded to incorporate other 'carrier' fluids that act as the background to the tracer. Again, the change in fluid properties, such as kinematic viscosity, will have a direct impact on flow properties such as the Reynolds number and therefore, affect the relative width. Fig. 6 shows how a simple ratio between the kinematic viscosities of the meta-model's liquid and the new liquid can lead to predictable R_w values, within some reasonable boundaries.

3.2. Correlation between experimental and CFD measurements

Comparison of simulated and experimental data is required to establish the relationship between the two models. Fig. 7 shows that experimental and simulated data follow a very similar trend with respect to T^*, however, there is a systematic offset between the two datasets. This offset can be accounted for by a combination of:

- Conductivity Probe measures within error limits ± 5 %. Each probe needs to be integrated into the system which adds additional tubing and system volume. This, in effect, will increase the residence time
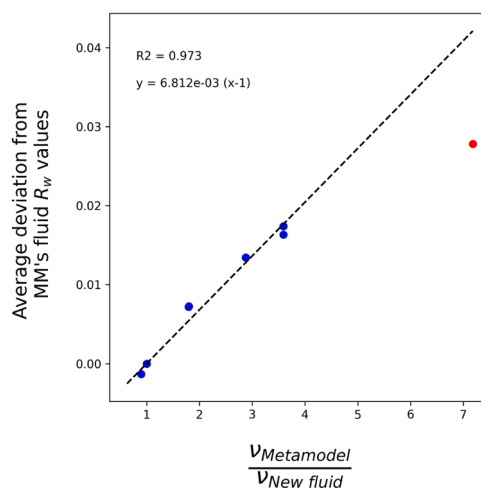

Fig. 6. RMSE between R_w values simulated using the MM's fluid and other fluids (negative sign was included for fluids with an x value lower than one). The x axis is the ratio between the kinematic viscosity of the MM's fluid ($\nu = 3.6 \, 10^{-6}$ m²/s) and that of the new fluid. The red circle does not follow the same trend as the rest, and thus, it was not included during the fitting of the curve or in the R2 score.
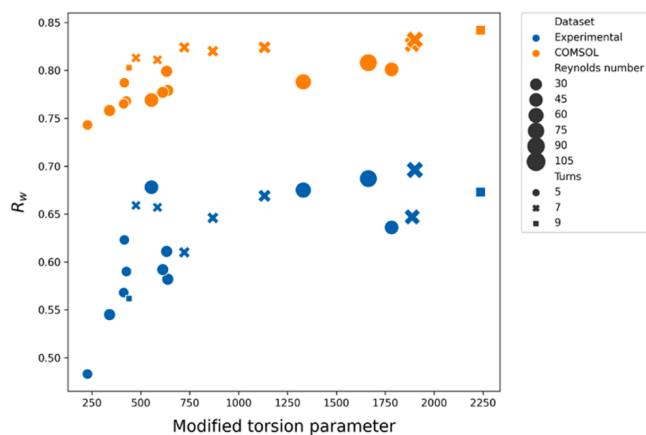
Fig. 7. Simulated and experimental R_w values of the same reactors as a function of the modified torsion parameter ($Re\pi d_c/p$). Simulated values were obtained using water as the fluid ($\rho = 998.2$ kg/m^3 and $\mu = 0.002$ kg/m/s) and H$^+$ ions as the tracer. The size and shape of the markers represent Re and n_t, respectively.

slightly and show lower performance (i.e. lower R_w values) compared to an ideal system.

- COMSOL simulation considers ideal reactor geometry. It measures mixing precisely from inlet to the outlet without considering additional volumes. The simulation does not take into account wall-fluid and wall-tracer intermolecular interactions which could be relevant due to the size of our reactors. Lastly, the simulation has been done using different tracer and concentrations which will have an effect on the resulting diffusion.
- The CAD model and printing materials used for producing reactors for experimental testing also have an effect, compared to the idealised model used in simulation. The curing process is essential for producing stable geometries, however overcuring can take place and internal channels could easily be up to ~ 5 % smaller than the CAD model. Surface roughness can vary across the length of a coil, due to the varying angle of incidence between the outside walls and the printing layer orientation. Lastly, post curing 3D printed resin will have a different surface finish to conventional tubing and this would not be captured in the simulation, which assumes there is no interaction with the internal walls.
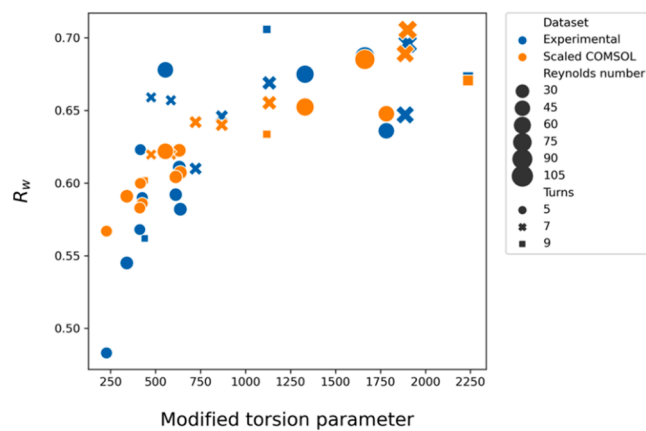
3.3. Predicting experimental values

Simulated and experimental values were obtained using the same fluid (water) but different tracers. CFD calculations used H$^+$ cations with a concentration of 0.25 mol/m^3, while experimental results were obtained using a 1 M NaCl solution. Based on CFD simulations, R_w depends on the tracer's diffusion constant and the ratio between R_w values simulated using different tracers can be fitted to an exponential equation of the form $y = Ae^{B\,Re} + 1$, where A and B are fitting coefficients and Re is the Reynolds number. Eq. (13) was fitted using 22 experimental values (Fig. S12).

$$R_{w,\mathrm{exp}} = \frac{R_{w,COMSOL}}{0.375\ e^{-0.00698Re} + 1} \tag{13}$$

As can be seen in Fig. 8, correcting the meta-model's predictions using Eq. (13) improves agreement with experimental data. A plot with the RMSE of the predictions can be found in the Supporting information (Fig. S13).

3.4. Meta-model for R_w of multilayer reactors

It has been observed that t_m and σ^2 scale linearly with the number of reactors connected in series (Parker et al., 2018). Therefore, the relative

Fig. 8. Simulated R_w values scaled using Eq. (13) and experimental R_w values as a function of the modified torsion parameter ($Re\pi D_c/pitch$).

width of the nth layer ($R_{w,n}$) can be predicted from a single-layer's tracer response if it is assumed that it follows a gaussian distribution and that $t_{m,n} = nt_m$ and $\sigma_n = \sqrt{n}\,\sigma$:

$$R_{w,n} = \frac{n - \sqrt{n}\,\frac{(1-\frac{R_{w,1}}{1+R_{w,1}})}{(1+\frac{R_{w,1}}{R_{w,1}})}}{n + \sqrt{n}\,\frac{(1-\frac{R_{w,1}}{1+R_{w,1}})}{(1+\frac{R_{w,1}}{R_{w,1}})}} \tag{14}$$

Predicted R_w values obtained using Eq. (13) are in very good agreement with simulated values of a 10-layer reactor with a RMSE of 0.002, as shown in Fig. 9. The full derivation of this equation can be found in the SI.

### 3.5. Experimental Measurements of Multi-layer Reactors

Fig. 10 compares experimental vs predicted R_w values of three multilayer reactors run at different flowrates. These reactors are referred as Reactor 2, Reactor 3 and Reactor 4 and the dimensions of Reactor 2 can be found in the Supporting information (Table S4).

R_w values for the first layer were obtained by testing each layer as a separate single-layer reactor and then calculating the average and standard deviation. Experimental values of the reactors tested at flowrates equal to 2.5 ml/min and 3.7 ml/min fall within the 95 % interval of confidence of the predictions, except for the 4th layer of Reactor 2 that is slightly overpredicted. On the other hand, experimental values
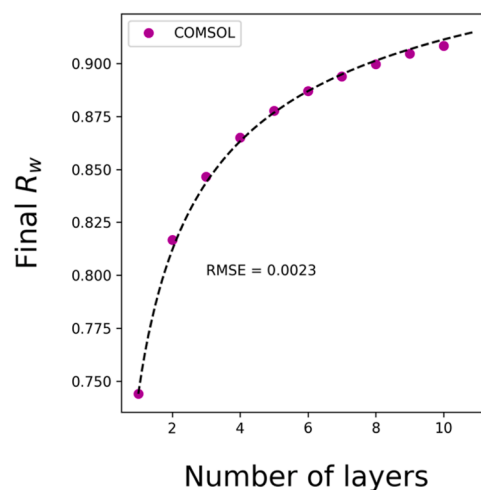
Fig. 9. R_w value against the number of layers in the final CFI reactor. The black dashed curve corresponds to the theoretical equation for R_w after n layers (Eq. (13)).
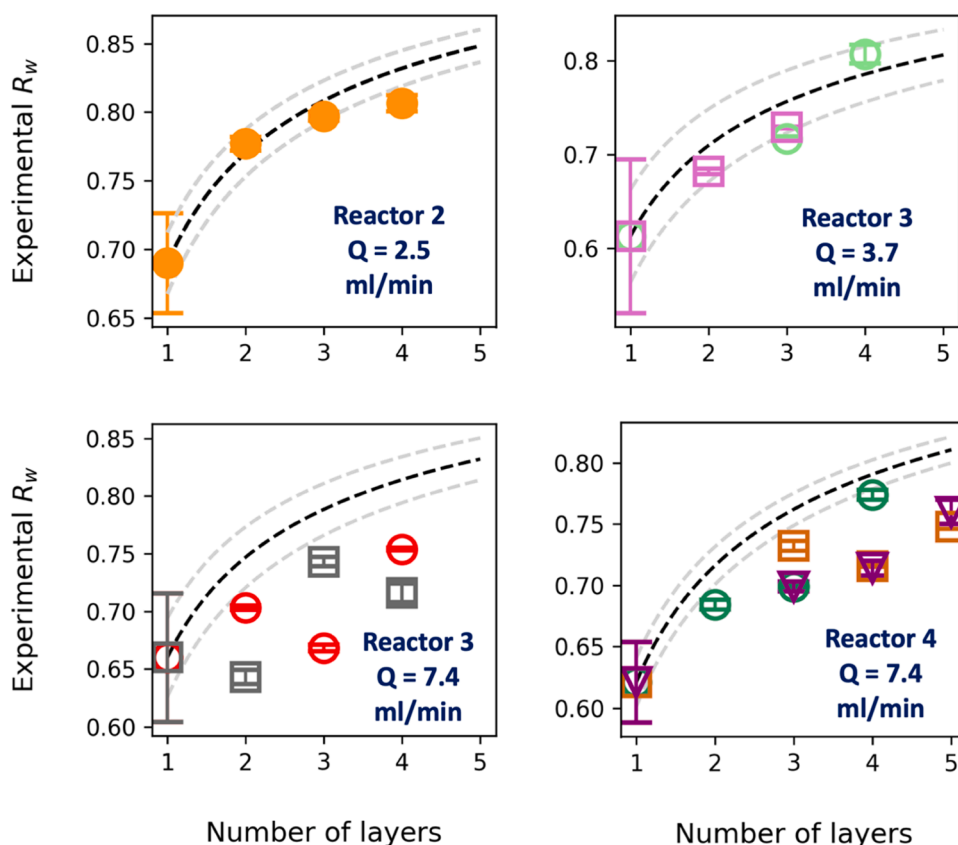
Fig. 10. Experimental R_w values as a function of the number of layers. The dashed black line corresponds to the theoretical equation for $R_{w,n}$ (Eq. (13)) and it was obtained using the first layer's R_w value. The grey dashed lines represent the 95 % confidence interval for the predicted values, and they were obtained by propagating the error associated to the first layer's R_w value. The markers with different shape (circle, square and triangle) and colours correspond to a repeated measurement of the reactor. For example, 2 independent experiments were carried out for Reactor 3 and thus, the red circles represent one of these runs while the grey squares represent the other measurement.

obtained using a flowrate of 7.4 ml/min do not follow the expected trend and are over predicted by Eq. (13). Therefore, extra measurements were carried out (represented using a different colour and marker), and it was noticed that some measurements were not consistent between the different repeats, especially for Reactor 3. This could be due to the location of the layers, since not all the layers had the same performance when tested separately, or the accuracy of the different probes. Further testing is needed to assess the performance of Eq. (13) at different flowrates and conditions.

3.6. Optimised reactor

Fig. 11 shows the reactor obtained using the optimisation routine explained in Section 2.4. This construct, from now on called Reactor 6, consists of 8 identical 3D printed layers and its parameters can be found in Table S4. This table also contains information about Reactor 2 since this reactor has the same volume and flowrate as Reactor 6. Like previous multi-layer reactor tests, each individually printed layer was tested as a single layer to ensure each layer was comparable and any deviations caused by fabrication defects could be excluded (Fig. S19). In testing, the optimised reactor performs better than Reactor 2 with a R_w value of 0.82 +/- 0.02 compared to 0.807 +/- 0.01 for Reactor 2. In comparison of the design parameters, this has been achieved by reduced the internal diameter, coil diameter and pitch, but increasing the number of turns and layers to maintain the same total volume.

4. Conclusions

This work demonstrates the potential of adaptive design to streamline the development of optimised reactor geometries, enhancing chemical production efficiency towards net-zero and environmental sustainability goals. Using the coiled flow inverter as a case study, we validated and optimised reactor performance through a combination of flow analysis, scaling, 3D printing, and experimental testing, supported by COMSOL CFD simulations. Our findings reveal that single-layer mixing performance correlates with anticipated improvements in multilayer designs, allowing us to derive an equation to estimate multilayer reactor efficiency based on single-layer data.

We developed an adaptive design model incorporating a meta-model for single-layer data and applied our derived equation to predict performance across multilayer reactor configurations. This enables process designers to select optimal constructs based on process constraints. Additionally, the adaptive design framework supports parametric customisation of the CFI reactor, allowing users to control key parameters and generate ready-to-print 3D geometries.

Our universal adaptive design workflow integrates high-fidelity CFD simulation and experimental data, offering a robust tool for designing and selecting high-performance, application-specific reactors.

CRediT authorship contribution statement

Anna Croft: Writing – review & editing, Supervision, Resources, Project administration, Funding acquisition. **Cameron J Brown:** Writing – review & editing, Supervision, Resources, Project administration, Funding acquisition, Conceptualization. **Ender Özcan:** Writing – review & editing, Supervision, Resources, Project administration, Funding acquisition. **Maria Cecilia Barrera:** Writing – review & editing, Writing – original draft, Visualization, Software, Methodology,
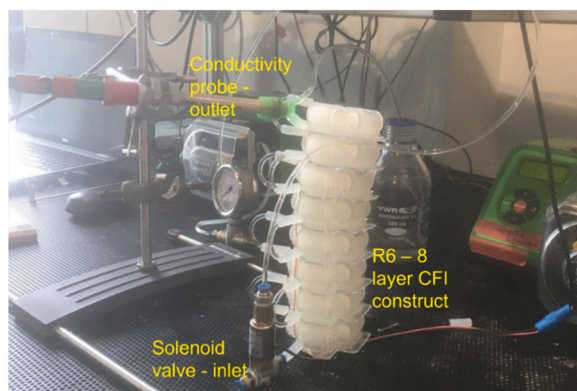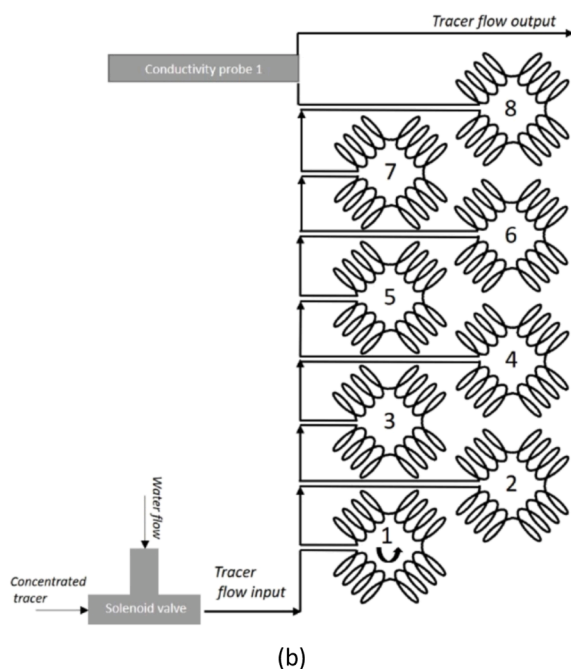
Fig. 11. (a) Set-up of reactor R6. This 8-layer construct is supplied by water and tracer via solenoid valve. Conductivity probe is installed on the reactor outlet and measures residence time distribution of the entire 8-layer construct. (b) Schematic shows 8-layer reactor design including solenoid valve and conductivity probe for inline RTD measurement.

Investigation, Formal analysis, Data curation, Conceptualization. **Alastair Florence:** Supervision, Project administration, Funding acquisition. **Damien Leech:** Writing – original draft, Visualization, Methodology, Investigation, Formal analysis, Data curation, Conceptualization. **Blair Johnston:** Supervision, Resources, Project administration, Funding acquisition. **Aleksandar Josifovic:** Writing – original draft, Visualization, Methodology, Investigation, Formal analysis, Data curation, Conceptualization. **John Robertson:** Supervision, Resources, Project administration, Funding acquisition. **Anita Tolouei:** Writing – review & editing, Validation, Supervision, Resources. **Gareth Alford:** Validation, Supervision, Resources, Funding acquisition. **Martin J. Wallace:** Validation, Supervision, Resources, Funding acquisition. **Nicholas Bennett:** Supervision, Resources, Project administration, Funding acquisition. **Ricky Wildman:** Writing – review & editing, Supervision, Resources, Project administration, Funding acquisition, Conceptualization. **Derek J. Irvine:** Writing – review & editing, Supervision, Resources, Project administration, Funding acquisition, Conceptualization.

Appendix A. Supporting information

Supplementary data associated with this article can be found in the online version at doi:10.1016/j.cherd.2024.11.040.

References

Bauer, J., Crook, C., Baldacchini, T., 2023. A sinterless, low-temperature route to 3D printnanoscale optical-grade glass. Science 380 (6648), 960–966.

Berg, S., van Wunnik, J., 2017. Shear rate determination from pore-scale flow fields. Transp. Porous Media 117 (2), 229–246.

Bobers, J., Gruhn, J., Höving, S., Pyka, T., Kockmann, N., 2020. Two-phase flow in a coiled flow inverter: process development from batch to continuous flow. Org. Process Res. Dev. 2094–2104.

David, L., Bayer, M.P., Lobedann, M., Schembecker, G., 2020. Simulation of continuous low pH viral inactivation inside a coiled flow inverter. Biotechnol. Bioeng. 1048–1062.

David, L., Maiser, B., Lobedann, M., Schwan, P., Lasse, M., Ruppach, H., Schembecker, G., 2019. Virus study for continuous low pH viral inactivation inside a coiled flow inverter. Biotechnol. Bioeng. 857–869.

Dragone, V., Sans, V., Rosnes, M.H., Kitson, P.J., Cronin, L., 2013. D-printed devices for continuous-flow organic chemistry. Beilstein J. Org. Chem. 3, 951–959.

Friedman, Jerome H., 1991. Multivariate adaptive regression splines. Ann. Stat. 19, 1–67.

Friedman, Jerome H., Roosen, Charles B., 1995. An introduction to multivariate adaptive regression splines. Stat. Methods Med. Res. 4, 197–217.

Gaddem, M.R., Ookawara, S., Nigam, K.D.P., Yoshikawa, S., Matsumoto, H., 2021. Numerical modeling of segmented flow in coiled flow inverter: hydrodynamics and mass transfer studies. Chem. Eng. Sci. 234, 116400.

Gaddem, M.R., Ookawara, S., Nigam, K.D., Yoshikawa, S., Matsumoto, H., 2022. Hydrodynamics and mixing in a novel design of compact microreactors: arc flow inverters. Chem. Eng. Process.-Process. Intensif. 180, 108770.

Grande, C.A., 2021. Compact reactor architectures designed with fractals. React. Chem. Eng. 1448–1453.

Grande, Carlos A., Didriksen, T., 2021. Production of customized reactors by 3D printing for corrosive and exothermic reactions. Ind. Eng. Chem. Res. 60 (46), 16720–16727.

Gürsel, I.V., Kurt, S.K., Aalders, J., Wang, Q., Noël, T., Nigam, K.D., Kockmann, N., Hessel, V., 2016. Utilization of milli-scale coiled flow inverter in combination with phase separator for continuous flow liquid–liquid extraction processes. Chem. Eng. J. 855–868.

Heidt, B., Rogosic, R., Bonni, S., Passariello-Jansen, J., Dimech, D., Lowdon, J.W., Arreguin-Campos, R., Steen Redeker, E., Eersels, K., Diliën, H., van Grinsven, B., Cleij, T.J., 2020. The liberalization of microfluidics: form 2 benchtop 3D printing as an affordable alternative to established manufacturing methods. Phys. Status Solidi (a) 1900935.

Jha, V.K., Sharma, L., Roy, S., Nigam, K.D.P., Bhaumik, S.K., 2020. Comparative assessment of mixing in compact coiled flow inverters under diffusion free laminar flow condition. Chem. Eng. Res. Des. 455–467.

Kateja, N., Nitika, N., Fadnis, R.S., Rathore, A.S., 2021. A novel reactor configuration for continuous virus inactivation. Biochem. Eng. J., 107885.

Klutz, S., Kurt, S.K., Lobedann, M., Kockmann, N., 2015. Narrow residence time distribution in tubular reactor concept for Reynolds number range of 10–100. Chem. Eng. Res. Des. 22–33.

Klutz, S., Lobedann, M., Bramsiepe, C., Schembecker, G., 2016. Continuous viral inactivation at low pH value in antibody manufacturing. Chem. Eng. Process.: Process Intensif. 88–101.

Kováts, P., Velten, C., Mansour, M., Thévenin, D., Zähringer, K., 2020. Mixing characterization in different helically coiled configurations by laser-induced fluorescence. Exp. Fluids 1–17.

Kumar, V., Gupta, P., Nigam, K.D.P., 2007b. Fluid flow and heat transfer in curved tubes with temperature-dependent properties. Ind. Eng. Chem. Res. 3226–3236.

Kumar, V., Mridha, M., Gupta, A.K., Nigam, K.D.P., 2007a. Coiled flow inverter as a heat exchanger. Chem. Eng. Sci. 2386–2396.

Kumar, V., Nigam, K.D.P., 2005. Numerical simulation of steady flow fields in coiled flow inverter. Int. J. Heat Mass Transf. 4811–4828.

Maier, M.C., Valotta, A., Hiebler, K., Soritz, S., Gavric, K., Grabner, B., Gruber-Woelfler, H., 2020. 3D printed reactors for synthesis of active pharmaceutical ingredients in continuous flow. Org. Process Res. Dev. 24 (10), 2197–2207.

Mandal, M.M., Aggarwal, P., Nigam, K.D.P., 2011. Liquid–liquid mixing in coiled flow inverter. Ind. Eng. Chem. Res. 50 (23), 13230–13235.

McDonough, J.R., Armett, J., Law, R., Harvey, A.P., 2019b. Coil-in-coil reactor: augmenting plug flow performance by combining different geometric features using 3D printing. Ind. Eng. Chem. Res. 21363–21371.

McDonough, J.R., Murta, S., Law, R., Harvey, A.P., 2019a. Oscillatory fluid motion unlocks plug flow operation in helical tube reactors at lower Reynolds numbers (Re ≤ 10). Chem. Eng. J. 643–657.

Mohammadi, S., Boodhoo, K.V., 2012. Online conductivity measurement of residence time distribution of thin film flow in the spinning disc reactor. Chem. Eng. J. 207, 885–894.

Mora Orozco, C.D.L., Jones, K.D., 2014. Evaluation of hydraulic residence time distribution (RTD) characterization and monitoring in a constructed channel wetland in South Texas. Environmental Sustainability Issues in the South Texas–Mexico Border Region. Springer, Dordrecht, pp. 159–177.

NationalInstruments, 2017. USB 6212 - Specification. [Online]. ⟨https://www.ni.com/pdf/manuals/375196d.pdf⟩.

Norman, Frederik, et al., 2023. Safety study of single-phase aerobic oxidations in 3D-printed reactors. Chem. Eng. Trans. 104, 91–96.

Orozco, R., Godfrey, S., Coffman, J., Amarikwa, L., Parker, S., Hernandez, L., Wachuku, C., Mai, B., Song, B., Hoskatti, S., Asong, J., Fiadeiro, M., 2017. Design, construction, and optimization of a novel, modular, and scalable incubation chamber for continuous viral inactivation. Biotechnol. Prog. 954–965.

Pal, S.K., Dhasmana, P., Nigam, K.D.P., Singh, V., 2019. Tuning of particle size in a helical coil reactor. Ind. Eng. Chem. Res. 3962–3971.

Parker, S.A., Amarikwa, L., Vehar, K., Orozco, R., Godfrey, S., Coffman, J., Shamlou, P., Bardliving, C.L., 2018. Design of a novel continuous flow reactor for low pH viral inactivation. Biotechnol. Bioeng. 606–616.

Pophali, A., Kajala, R., Ali, H., Verma, N., Nigam, K.D.P. 2022. Reaction Chemistry & Engineering.

Rossi, D., Gargiulo, L., Valitov, G., Gavriilidis, A., Mazzei, L., 2017. Experimental characterization of axial dispersion in coiled flow inverters. Chem. Eng. Res. Des. 120, 159–170.

Roth, E., Kessler, M., Fabre, B., Accary, A., 1999. Sodium chloride stimulus-response experiments in spiral wound reverse osmosis membranes: a new method to detect fouling. Desalination 121 (2), 183–193.

Savitzky, Abraham, Marcel, J.E.Golay, 1964. Smoothing and differentiation of data by simplified least squares procedures. Anal. Chem. 1627–1639.

Saxena, A.K., Nigam, K.D.P., 1983. Effect of coil pitch and cross-sectional ellipticity on RTD for diffusion-free laminar flow in coiled tubes. Chem. Eng. Commun. 277–289.

Saxena, A.K., Nigam, K.D.P., 1984. Coiled configuration for flow inversion and its effect on residence time distribution. AIChE J. 363–368.

Schael, F., Steup, B., Rojahn, P., Nigam, K.D.P., 2024. Chemie Ingenieur Technik.

Schmalenberg, Mira, Hohmann, Lukas, Kockmann, Norbert, 2018. Miniaturized tubular cooling crystallizer with solid-liquid flow for process developmen. In: Proceedings of the International Conference of Nanochannels, Microchannels, and Minichannels. American Society of Mechanical Engineers, Dubrovnik, Croatia.

Schmalenberg, M., Krieger, W., Kockmann, N., 2019. Modular coiled flow inverter with narrow residence time distribution for process development and production. Chem. Ing. Tech. 567–575.

Sharma, A.K., Agarwal, H., Pathak, M., Nigam, K.D.P., Rathore, A.S., 2016. Continuous refolding of a biotech therapeutic in a novel Coiled Flow Inverter Reactor. Chem. Eng. Sci. 140, 153–160.

Soni, S., Sharma, L., Meena, P., Roy, S., Nigam, K.D.P., 2019. Compact coiled flow inverter for process intensification. Chem. Eng. Sci. 312–324.

Toledo, Mettler, 2013. M800 Transmitter Series. [Online]. ⟨https://www.mt.com/dam/MTPRO/PDF/DS/DS_M800_Series_en_30112337_Oct13.pdf⟩.

Toledo, Mettler, 2017. InPro 7100i. Data sheet. [Online]. ⟨https://www.pharmaceutical-business-review.com/wp-content/uploads/2020/03/DS_ConductivitySensor_InPro7100_en_52900359_Jul17.pdf⟩.

Tomar, S.S., Verma, N., Nigam, K.D.P., 2023. Adsorptive desulfurization of thiophene using Cu-CNF slurry in a coiled flow inverter with recycling. Chem. Eng. Sci. 281, 119172.

Vashisth, S., Nigam, K.D.P., 2008. Liquid-phase residence time distribution for two-phase flow in coiled flow inverter. Ind. Eng. Chem. Res. 3630–3638.

Wu, K.J., Torrente-Murciano, L., 2018. Continuous synthesis of tuneable sized silver nanoparticles via a tandem seed-mediated method in coiled flow inverter reactors. React. Chem. Eng. 267–276.